tri-NaCitrate and 20% PEG 3350, at a final pH of 7.4 (PEG/Ion Screen, Hampton Research, San Diego, California) within two weeks at 4 °C. Intact complex was verified by SDS–polyacrylamide gel electrophoresis of washed crystals (see Supplementary Information). Data were collected from a single frozen crystal, cryoprotected in 28.5% PEG 4000 and 10% PEG 400, at beamline 9.6 at the SRS Daresbury, UK.

The data were processed using MOSFLM[24] and merged using SCALA[25] from the CCP4 package[26] (Table 1) The molecular replacement solution for α_1-antitrypsin in the complex was obtained using AMORE[27] and the structure of cleaved α_1-antitrypsin[28] as the search model. Conventional molecular replacement searches failed to place a model of intact trypsin[29] in the complex, although maps calculated with phases from α_1-antitrypsin alone showed clear density for the ordered portion of trypsin (Fig. 3 and Supplementary Information). It was immediately apparent that density was only present for about half of the volume expected to be occupied by intact trypsin. A search model comprising trypsin residues 27–124 and 230–245 was orientated using AMORE to compute a domain rotation function[30] against structure factors corresponding to a sphere of the ordered density, which were calculated using the program GHKL (L. Tong, unpublished data). The position of the oriented model relative to α_1-antitrypsin was determined with AMORE using the original diffraction data. The entire model of trypsin was superimposed on the fragment and then truncated to the limits of the electron density to provide an initial model of the complex. The truncated model, to our surprise, was nearly complete in accounting for the ordered structure contributing to the diffraction data, despite including only about 50% of the trypsin residues. In fact, the amount of ordered density changed little throughout the course of refinement. Completeness of this model was estimated at 99% by a σ_A-plot computed in the program SIGMAA[31]. The model comprising α_1-antitrypsin alone was estimated to be 83% complete, whereas α_1-antitrypsin comprises only 62% of the mass of the complex (σ_A-plots are included as Supplementary Information). The final molecular model was achieved through an iterative procedure of rebuilding using XtalView and refinement in CNS[32] using a maximum likelihood target[33]. Statistics for data processing, refinement and for the final model are given in Table 1. Figures were made using the programs Molscript[34], Bobscript[35] and Raster3D[36].

Received 10 May; accepted 2 August 2000.

1. Potempa, J., Korzus, E. & Travis, J. The serpin superfamily of proteinase inhibitors: structure, function, and regulation. *J. Biol. Chem.* **269,** 15957–15960 (1994).
2. Laskowski, M. & Qasim, M. A. What can the structures of enzyme-inhibitor complexes tell us about the structures of enzyme substrate complexes? *Biochim. Biophys. Acta* **1477,** 324–337 (2000).
3. Loebermann, H., Tokuoka, R., Deisenhofer, J. & Huber, R. Human alpha 1-proteinase inhibitor. Crystal structure analysis of two crystal modifications, molecular model and preliminary analysis of the implications for function. *J. Mol. Biol.* **177,** 531–557 (1984).
4. Huber, R. & Bode, W. Structural basis of the activation and action of trypsin. *Acc. Chem. Res.* **11,** 114–122 (1978).
5. Kaslik, G., Patthy, A., Balint, M. & Graf, L. Trypsin complexed with alpha 1-proteinase inhibitor has an increased structural flexibility. *FEBS Lett.* **370,** 179–183 (1995).
6. Stavridi, E. S. *et al.* Structural change in alpha-chymotrypsin induced by complexation with alpha 1-antichymotrypsin as seen by enhanced sensitivity to proteolysis. *Biochemistry* **35,** 10608–10615 (1996).
7. Huber, R. & Carrell, R. W. Implications of the three-dimensional structure of alpha 1-antitrypsin for structure and function of serpins. *Biochemistry* **28,** 8951–8966 (1989).
8. Elliott, P. R., Abrahams, J. P. & Lomas, D. A. Wild-type alpha 1-antitrypsin is in the canonical inhibitory conformation. *J. Mol. Biol.* **275,** 419–425 (1998).
9. Wright, H. T. & Scarsdale, J. N. Structural basis for serpin inhibitor activity. *Proteins* **22,** 210–225 (1995).
10. Stratikos, E. & Gettins, P. G. Formation of the covalent serpin–proteinase complex involves translocation of the proteinase by more than 70 A and full insertion of the reactive center loop into beta-sheet A. *Proc. Natl Acad. Sci. USA* **96,** 4808–4813 (1999).
11. Fa, M. *et al.* The structure of a serpin-proteinase complex revealed by intramolecular distance measurements using donor-donor energy migration and mapping of interaction sites. *Structure* **8,** 397–405 (2000).
12. Picard, V., Marque, P. E., Paolucci, F., Aiach, M. & Le Bonniec, B. F. Topology of the stable serpin–protease complexes revealed by an autoantibody that fails to react with the monomeric conformers of antithrombin. *J. Biol. Chem.* **274,** 4586–4593 (1999).
13. Carrell, R. W. & Owen, M. C. Plakalbumin, alpha 1-antitrypsin, antithrombin and the mechanism of inflammatory thrombosis. *Nature* **317,** 730–732 (1985).
14. Stein, P. E. *et al.* Crystal structure of ovalbumin as a model for the reactive centre of serpins. *Nature* **347,** 99–102 (1990).
15. Engh, R. A., Huber, R., Bode, W. & Schulze, A. J. Divining the serpin inhibition mechanism: a suicide substrate 'spring'? *Trends Biotechnol.* **13,** 503–510 (1995).
16. Gooptu, B. *et al.* Inactive conformation of the serpin alpha(1)-antichymotrypsin indicates two-stage insertion of the reactive loop: implications for inhibitory function and conformational disease. *Proc. Natl Acad. Sci. USA* **97,** 67–72 (2000).
17. Herve, M. & Ghelis, C. Conformational stability of the covalent complex between elastase and alpha 1-proteinase inhibitor. *Arch. Biochem. Biophys.* **285,** 142–146 (1991).
18. Olson, S. T. *et al.* Role of the catalytic serine in the interactions of serine proteinases with protein inhibitors of the serpin family. Contribution of a covalent interaction to the binding energy of serpin–proteinase complexes. *J. Biol. Chem.* **270,** 30007–30017 (1995).
19. Plotnick, M. I., Mayne, L., Schechter, N. M. & Rubin, H. Distortion of the active site of chymotrypsin complexed with a serpin. *Biochemistry* **35,** 7586–7590 (1996).
20. Gils, A. & Declerck, P. J. Structure-function relationships in serpins: current concepts and controversies. *Thromb. Haemost.* **80,** 531–541 (1998).
21. Harrop, S. J. *et al.* The crystal structure of plasminogen activator inhibitor 2 at 2. 0 Å resolution: implications for serpin function. *Struct. Fold Des.* **7,** 43–54 (1999).
22. Holmes, W. E. *et al.* Alpha 2-antiplasmin Enschede: alanine insertion and abolition of plasmin inhibitory activity. *Science* **238,** 209–211 (1987).
23. Bode, W. & Huber, R. Structural basis of the endoproteinase-protein inhibitor interaction. *Biochim. Biophys. Acta* **1477,** 241–252 (2000).
24. Leslie A. W. G. in *Joint CCP4 and ESF-EACMB Newsletter on Protein Crystallography* vol. 26 (Daresbury Laboratory, Warrington, 1992).
25. Evans P. R. in *Proceedings of the CCP4 Study Weekend. Data Collection and Processing* (eds Sawyer, L., Isaacs, N. & Bailey, S.) 114–122 (Daresbury Laboratory, 1993).
26. Collaborative Computational Project Number 4. The CCP4 suite: programs for protein crystallography. *Acta Crystallogr.* **50,** 760–763 (1994).
27. Navaza, J. AMORE - An automated package for molecular replacement. *Acta Cryst. A* **50,** 157–163 (1994).
28. Engh, R. *et al.* The S variant of human alpha 1-antitrypsin, structure and implications for function and metabolism. *Protein Eng.* **2,** 407–415 (1989).
29. Lee, S. L. New inhibitors of thrombin and other trypsin-like proteases: hydrogen bonding of an aromatic cyano group with a backbone amide of the P1 binding site replaces binding of a basic side chain. *Biochemistry* **36,** 13180–13186 (1997).
30. Colman, P. M., Fehlhammer, H. & Bartles, K. in *Crystallographic Computing Techniques* (eds Ahmed, F. R., Huml, K. & Sedlacek, B.) 248–258 (Munksgaard, Copenhagen, 1976).
31. Read, R. J. Improved Fourier coefficients for maps using phases from partial structures with errors. *Acta Cryst. A* **42,** 140–149 (1986).
32. Brunger, A. T. *et al.* Crystallography & NMR system: A new software suite for macromolecular structure determination. *Acta Cryst. D* **54,** 905–921 (1998).
33. Pannu, N. S. & Read, R. J. Improved structure refinement through maximum likelihood. *Acta Cryst. A* **52,** 659–668 (1996).
34. Kraulis, P. J. MOLSCRIPT: a program to produce both detailed and schematic plots of protein structures. *J. Appl. Crystallogr.* **24,** 946–950 (1991).
35. Esnouf, R. Further additions to MolScript version 1.4, including reading and contouring of electron-density maps. *Acta Crystallogr. D* **55,** 938–940 (1999).
36. Merritt, E. A. & Bacon, D. J. Raster3D: photorealistic molecular graphics. *Methods Enzymol.* **277,** 505–524 (1997).

Supplementary information is available on *Nature*'s World-Wide Web site (http://www.nature.com) or as paper copy from the London editorial office of *Nature*.

Acknowledgements

We thank our colleagues, N. Pannu for advice throughout; D. Lomas for reading the paper; A. Lesk and P. Stein for discussions; and K. Belzar for support. This work was supported by grants from the Wellcome Trust, the European Community and the National Institutes of Health (J.A.H.).

Correspondence and requests for materials should be addressed to J.A.H. (e-mail: jah52@cam.ac.uk) or R.W.C. (e-mail: rwc1000@cam.ac.uk). Atomic coordinates have been deposited in the Protein Data Bank under accession code 1EZX.

errata

Intraprotein radical transfer during photoactivation of DNA photolyase

Corrine Aubert, Marten H. Vos, Paul Mathis, André P. M. Eker & Klaus Brettel

Nature **405,** 586–590 (2000).

Figure 5 of this paper contained an error. The lower right-hand box in the reaction scheme, which read 'FADH$^-$ TrpH TrpH TrpH$^{\bullet}$', should have read 'FADH$^-$ TrpH TrpH Trp$^{\bullet}$'. □

Neural synchrony correlates with surface segregation rules

Miguel Castelo-Branco, Rainer Goebel, Sergio Neuenschwander & Wolf Singer

Nature **405,** 685–689 (2000).

In Fig. 1b of this Letter, the scale bar for the repetitive fields should be half as large as it was printed. In Fig. 1c, the label that reads PMLS should read A18. □

possibility that, at least in some contexts, accessibility regulation could involve the modulation of putative RSS-specific *trans*-acting factors that promote RAG-1/2 access. □

Methods

Generation of targeted ES cells and mutant mice

We generated pDJβ2KO by subcloning the 4-kb *Kpn*I–*Alw*NI 5′ and 3-kb *Xba*I–*Spe*I 3′ homology regions that flank the DJβ2 gene cluster into the previously described pLNTK targeting vector[29]. The construction of the targeting vectors for the M3, M4 and M5 mutations and the generation of ES cells with $J\beta1^{M3}$, $J\beta1^{M3}$, $J\beta1^{M4}$ and $J\beta1^{M5}$ mutant alleles are described in the Supplementary Information. Transfection and selection of ES cells were carried out as described[29]. Chimaeric mice were generated by RAG-2-deficient blastocyst complementation[19].

Southern and northern blot analyses

Southern and northern blot analyses were carried out as described[29]. Probes A and C were 0.8-kb *Drd*I–*Drd*I and 0.7-kb *Afl*II–*Hae*II TCRβ genomic DNA fragments, respectively. The Jβ1 probe was a 2-kb *Pst*I genomic DNA fragment. Glyceraldehyde phosphate dehydrogenase and complementary CD3ε DNA probes have been described previously[29].

PCR analyses

The Vβ primer set (PV) has been described previously[30] with the exception of the Vβ14 primer: 5′-GGCAAGCAAGCTGGTGTGT-3′. The sequences of the remaining primers are as follows: P2, 5′-CCTGACTTCCACCCGAGGTT-3′; P3, 5′-CCTTCCTTATCTT-CAACTC-3′; P4, 5′-AAGGGACGACTCTGTCTT-3′; PR2, 5′-CATCCTTCCTCTGAT-TAC-3′. PCR was carried out as described[30] at 92°, 90 s; 60°, 150 s; 72°, 60 s for 30 cycles.

Flow cytometric analysis and cell sorting

Flow cytometric analysis of thymocytes for CD4 and CD8 expression was carried out as described[29]. Cell sorting was carried out by pretreatment of thymocytes with anti-CD4 and anti-CD8 and complement followed by sorting of $CD25^+/CD4^-/CD8^-$ thymocytes on an Epics MoFlow sorter.

Received 8 March; accepted 19 April 2000.

1. Tonegawa, S. Somatic generation of antibody diversity. *Nature* **302,** 575–581 (1983).
2. Weaver, D. T. V(D)J recombination and double-strand break repair. *Adv. Immunol.* **58,** 29–85 (1995).
3. Jeggo, P. A. Identification of genes involved in repair of DNA double-strand breaks in mammalian cells. *Radiat. Res.* **150,** 580–591 (1998).
4. Eastman, Q. M., Leu, T. M. & Schatz, D. G. Initiation of V(D)J recombination *in vitro* obeying the 12/23 rule. *Nature* **380,** 85–88 (1996).
5. van Gent, D. C., Ramsden, D. A. & Gellert, M. The RAG1 and RAG2 proteins establish the 12/23 rule in V(D)J recombination. *Cell* **85,** 107–113 (1996).
6. Uematsu, Y. *et al.* In transgenic mice the introduced functional T cell receptor beta gene prevents expression of endogenous beta genes. *Cell* **52,** 831–841 (1988).
7. Ferrier, P. *et al.* Separate elements control DJ and VDJ rearrangement in a transgenic recombination substrate. *EMBO J.* **9,** 117–125 (1990).
8. Davis, M. M. & Bjorkman, P. J. T-cell antigen receptor genes and T-cell recognition. *Nature* **334,** 395–402 (1988).
9. Nadel, B., Tang, A., Escuro, G., Lugo, G. & Feeney, A. J. Sequence of the spacer in the recombination signal sequence affects V(D)J rearrangement frequency and correlates with nonrandom Vκ usage *in vivo*. *J. Exp. Med.* **187,** 1495–1503 (1998).
10. Hesse, J. E., Lieber, M. R., Mizuuchi, K. & Gellert, M. V(D)J recombination: a functional definition of the joining signals. *Genes Dev.* **3,** 1053–1061 (1989).
11. Gerstein, R. M. & Lieber, M. R. Coding end sequence can markedly affect the initiation of V(D)J recombination. *Genes Dev.* **7,** 1459–1469 (1993).
12. Boubnov, N. V., Wills, Z. P. & Weaver, D. T. Coding sequence composition flanking either signal element alters V(D)J recombination efficiency. *Nucleic Acids Res.* **23,** 1060–1067 (1995).
13. Ramsden, D. A. & Wu, G. E. Mouse κ light-chain recombination signal sequences mediate recombination more frequently than do those of λ light chain. *Proc. Natl Acad. Sci. USA* **88,** 10721–10725 (1991).
14. Wei, Z. & Lieber, M. R. Lymphoid V(D)J recombination. Functional analysis of the spacer sequence within the recombination signal. *J. Biol. Chem.* **268,** 3180–3183 (1993).
15. Connor, A. M. *et al.* Mouse V_H7183 recombination signal sequences mediate recombination more frequently than those of V_HJ558. *J. Immunol.* **155,** 5268–5272 (1995).
16. Akira, S., Okazaki, K. & Sakano, H. Two pairs of recombination signals are sufficient to cause immunoglobulin V-(D)-J joining. *Science* **238,** 1134–1138 (1987).
17. Gauss, G. H. & Lieber, M. R. The basis for the mechanistic bias for deletional over inversional V(D)J recombination. *Genes Dev.* **6,** 1553–1561 (1992).
18. VanDyk, L. F., Wise, T. W., Moore, B. B. & Meek, K. Immunoglobulin D_H recombination signal sequence targeting: effect of D_H coding and flanking regions and recombination partner. *J. Immunol.* **157,** 4005–4015 (1996).
19. Chen, J., Lansford, R., Stewart, V., Young, F. & Alt, F. W. RAG-2-deficient blastocyst complementation: an assay of gene function in lymphocyte development. *Proc. Natl Acad. Sci. USA* **90,** 4528–4532 (1993).
20. Willerford, D. M., Swat, W. & Alt, F. W. Developmental regulation of V(D)J recombination and lymphocyte differentiation. *Curr. Opin. Genet. Dev.* **6,** 603–609 (1996).
21. Sikes, M. L., Suarez, C. C. & Oltz, E. M. Regulation of V(D)J recombination by transcriptional promoters. *Mol. Cell. Biol.* **19,** 2773–2781 (1999).
22. Doty, R. T., Xia, D., Nguyen, S. P., Hathaway, T. R. & Willerford, D. M. Promoter element for transcription of unrearranged T-cell receptor beta-chain gene in pro-T cells. *Blood* **93,** 3017–3025 (1999).
23. Whitehurst, C. E., Chattopadhyay, S. & Chen, J. Control of V(D)J recombinational accessibility of the Dβ1 gene segment at the TCRβ locus by a germline promoter. *Immunity* **10,** 313–322 (1999).
24. Ramsden, D. A., Baetz, K. & Wu, G. E. Conservation of sequence in recombination signal sequence spacers. *Nucleic Acids Res.* **22,** 1785–1796 (1994).
25. Yancopoulos, G. D. *et al.* Preferential utilization of the most J_H-proximal V_H gene segments in pre-B-cell lines. *Nature* **311,** 727–733 (1984).
26. Jouvin-Marche, E. *et al.* Genomic organization of the T cell receptor V_α family. *EMBO J.* **9,** 2141–2150 (1990).
27. Alt, F. W. *et al.* Ordered rearrangement of immunoglobulin heavy chain variable region segments. *EMBO J.* **3,** 1209–1219 (1984).
28. Rock, E. P., Sibbald, P. R., Davis, M. M. & Chien, Y.-H. CRD3 length in antigen-specific immune receptors. *J. Exp. Med.* **179,** 323–328 (1994).
29. Sleckman, B. P., Bardon, C. G., Ferrini, R., Davidson, L. & Alt, F. W. Function of the TCR alpha enhancer in αβ and γδ T cells. *Immunity* **7,** 505–515 (1997).
30. Gärtner, F. *et al.* Immature thymocytes employ distinct signaling pathways for allelic exclusion versus differentiation and expansion. *Immunity* **10,** 537–546 (1999).
31. Sleckman, B. P. *et al.* Mechanisms that direct ordered assembly of T-cell receptor β locus V, D, and J gene segments. *Proc. Natl Acad. Sci. USA.* (in the press).

Supplementary information is available on *Nature*'s World-Wide Web site (http://www.nature.com) or as paper copy from the London editorial office of *Nature*.

Acknowledgements

We thank O. Kanagawa and K. Murphy for advice and discussions and D. Fenoglio for assistance on cell sorting. This work is supported in part by the National Institutes of Health (F.W.A.). B.P.S. is a recipient of a Career Development Award from the Burroughs Wellcome Fund. C.H.B. was a fellow of the Irvington Institute for Immunological Research. F.G. is an associate of the Howard Hughes Medical Institute. F.W.A. is an investigator of the Howard Hughes Medical Institute.

Correspondence and requests for materials should be addressed to B.P.S. (e-mail: sleckman@immunology.WUSTL.edu).

Intraprotein radical transfer during photoactivation of DNA photolyase

Corinne Aubert*, Marten H. Vos†, Paul Mathis*, André P. M. Eker‡ & Klaus Brettel*

** Section de Bioénergétique (CNRS URA 2096), CEA Saclay, 91191 Gif-sur-Yvette Cedex, France*
† INSERM U451, Laboratoire d'Optique Appliquée, Ecole Polytechnique-ENSTA, 91761 Palaiseau Cedex, France
‡ Department of Cell Biology and Genetics, Medical Genetics Centre, Erasmus University Rotterdam, PO Box 1738, 3000 DR Rotterdam, The Netherlands

Amino-acid radicals play key roles in many enzymatic reactions[1]. Catalysis often involves transfer of a radical character within the protein, as in class I ribonucleotide reductase where radical transfer occurs over 35 Å, from a tyrosyl radical to a cysteine[1–3]. It is currently debated whether this kind of long-range transfer occurs by electron transfer, followed by proton release to create a neutral radical, or by H-atom transfer, that is, simultaneous transfer of electrons and protons[4–7]. The latter mechanism avoids the energetic cost of charge formation in the low dielectric protein[4,5], but it is less robust to structural changes than is electron transfer[7]. Available experimental data do not clearly discriminate between these proposals. We have studied the mechanism of photoactivation (light-induced reduction of the flavin adenine dinucleotide cofactor) of *Escherichia coli* DNA photolyase[8–10] using time-resolved absorption spectroscopy. Here we show that the excited flavin adenine dinucleotide radical abstracts an electron from a nearby tryptophan in 30 ps. After subsequent electron transfer along a chain of three tryptophans,

the most remote tryptophan (as a cation radical) releases a proton to the solvent in about 300 ns, showing that electron transfer occurs before proton dissociation. A similar process may take place in photolyase-like blue-light receptors.

DNA photolyase catalyses the repair of major ultraviolet-induced DNA lesions, cyclobutane pyrimidine dimers or (6-4)-photoproducts, using the energy of near-ultraviolet light[8,10] (Fig. 1). This enzyme, which is found in a variety of organisms ranging from bacteria to multicellular eukaryotes, consists of a single polypeptide with a relative molecular mass of ~55,000. It binds a flavin adenine dinucleotide (FAD) molecule as the essential catalytic cofactor, and it only functions when the FAD is fully reduced ($FADH^-$). In isolated DNA photolyases, the FAD is typically in the inactive semireduced radical state $FADH^\bullet$, but it can be easily reduced to the catalytically active $FADH^-$ state by illumination with visible light in the presence of an exogenous electron donor, a process called photoactivation (Fig. 1).

The mechanism of photoactivation has been studied for *E. coli* photolyase[9,11,12]. Excited $FADH^\bullet$ oxidizes the solvent-accessible tryptophan W306, and exogenous electron donors then reduce the oxidized tryptophan (in competition with charge recombination occurring in about 10 ms; see Fig. 1, broken arrow) and thus stabilize the $FADH^-$ state as required for the DNA repair function of the enzyme. We used absorption spectroscopy in the picosecond to millisecond time domain after selective excitation of $FADH^\bullet$ by red laser flashes to study in detail the mechanism of radical transfer from $FADH^\bullet$ to tryptophan (TrpH; H denotes the N1 proton) in recombinant *E. coli* photolyase[13].

The final protonation state of the tryptophanyl radical was determined from absorption changes accompanying the recombination between $FADH^-$ and the tryptophanyl radical in the absence of an exogenous electron donor (Fig. 2). Throughout the 400–645-nm spectral range studied, we observed absorbance changes appearing within 5 μs and relaxing exponentially because of charge recombination with a time constant τ = 17 ms (at pH 7.4). From the spectrum of these absorbance changes (Fig. 2a, spectrum A), we conclude that the tryptophanyl radical is in the unprotonated (neutral) state ($Trp^\bullet$) at times later than 5 μs after excitation of $FADH^\bullet$, because the difference between spectrum A and the ($FADH^-$–$FADH^\bullet$) difference spectrum B is inconsistent with the absorption spectrum of the protonated (cation) radical $TrpH^{\bullet+}$, but agrees well with that of $Trp^\bullet$ (Fig. 2b). The recombination kinetics accelerated strongly upon lowering the pH (τ = 7 ms at pH 6.5 and 0.9 ms at pH 5.4; see Fig. 2a, inset). The most straightforward explanation for the acceleration is that recombination requires $Trp^\bullet$ reprotonation. The presence of $Trp^\bullet$ is also consistent with the acidity of $TrpH^{\bullet+}$, which has a pK ≈ 4 in water[14,15]. An electron transfer from a tyrosine residue to $Trp^\bullet$ as observed recently in photolyase from *Anacystis nidulans*[16,17] was not detectable in photolyase from *E. coli*.

To establish whether $Trp^\bullet$ is formed by hydrogen atom transfer or by electron transfer and subsequent deprotonation, we measured the kinetics of flash-induced absorbance changes in the nanosecond timescale in the 300–645-nm range where deprotonation of $TrpH^{\bullet+}$ is expected to give characteristic absorbance changes (see Fig. 2b). A typical signal measured at 580 nm is shown in the inset of Fig. 3a (trace H_2O). A fast, instrument-limited bleaching is followed by a further bleaching with $\tau \approx 300$ ns. The same kinetic components were observed at all other wavelengths studied. The spectrum of the amplitude of the 300-ns phase (Fig. 3a, spectrum A - B) agrees well

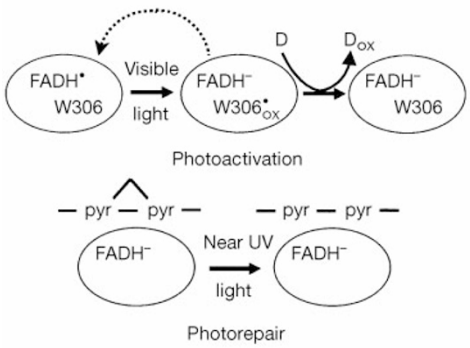

Figure 1 Outline of the photoactivation (top panel) and photorepair (bottom panel) reactions of DNA photolyase. See text for details. D, exogenous electron donor; pyr, pyrimidine in DNA.

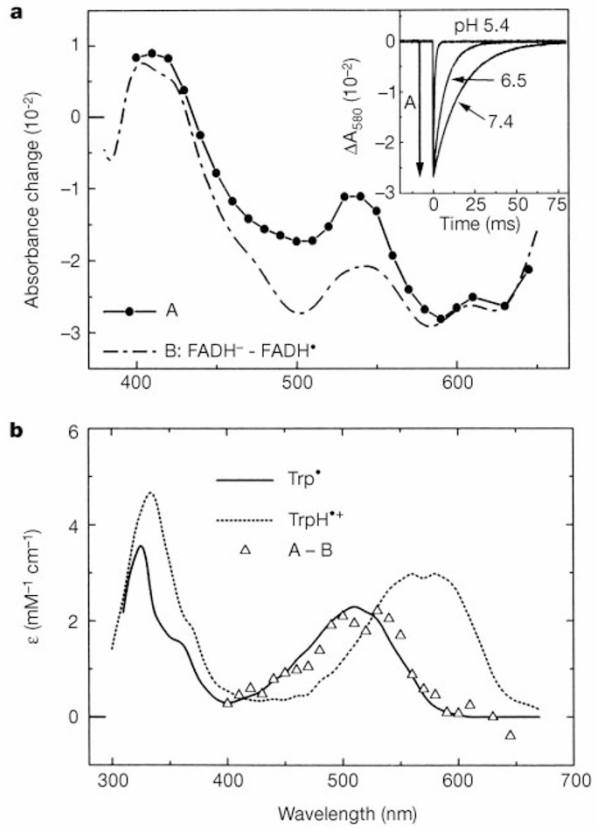

Figure 2 Evidence for a deprotonated tryptophanyl radical ($Trp^\bullet$). **a**, Trace A, spectrum of flash-induced absorbance changes decaying with τ = 17 ms (pH 7.4), obtained from kinetic traces like that at pH 7.4 and 580 nm in the inset. Trace B, ($FADH^-$–$FADH^\bullet$) difference spectrum in *E. coli* photolyase, obtained by subtracting absorption spectra recorded using a Kontron (model UV 922) spectrophotometer before and after saturating illumination with continuous light (540–650 nm) in the presence of 5 mM 1,4-dithiothreitol as exogenous electron donor. Spectrum B was normalized to spectrum A at ~630 nm. Inset, pH effect on the kinetics of the flash-induced absorbance change at 580 nm. The samples contained about 30 μM photolyase, 200 mM NaCl, 15% (w/w) glycerol and 20 mM buffer (pH 7.4, Tris-HCl; pH 5.4 and pH 6.5, MES). Dithiothreitol was only added in spectrum B. Absorbance changes were recorded with a resolution of 5 μs using continuous monitoring light[16]. The samples were excited by 7-ns dye laser pulses of ~30 mJ cm^{-2} at 635 nm (for monitoring wavelengths $\lambda_m \leq 610$ nm) or ~20 mJ cm^{-2} at 675 nm (for $\lambda_m \geq 610$ nm). Amplitudes in A were corrected for slight degradation of the samples during data collection and for the lower efficiency of the 675-nm excitation, using control measurements at 580 nm and 610 nm. **b**, Comparison of the difference between A and B (triangles) with absorption spectra of $Trp^\bullet$ and $TrpH^{\bullet+}$ in aqueous solution (taken from ref. 15). The (A – B) difference spectrum was normalized to the other spectra at their isosbestic point (527 nm). The samples were kept at 10 °C during all spectroscopic measurements.

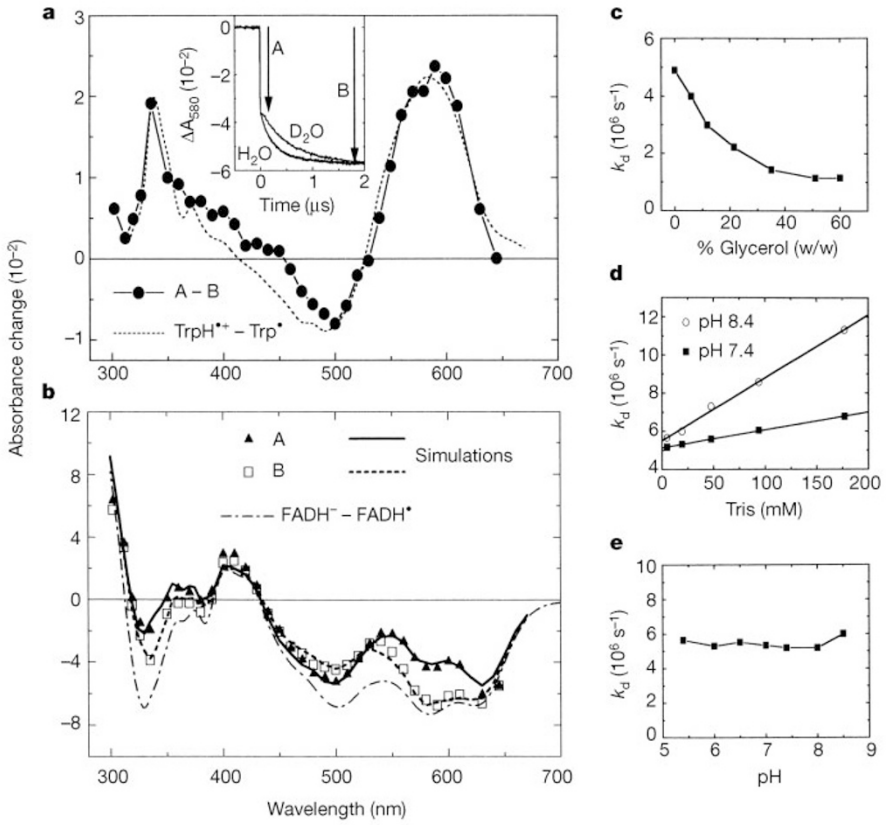

Figure 3 Monitoring the $TrpH^{\bullet+}$ deprotonation in the nanosecond time range. **a**, Circles, spectrum of the amplitude of the $\tau \approx 300$-ns phase obtained from flash-induced absorbance changes like the 'H_2O' trace at 580 nm in the inset. Broken line, ($TrpH^{\bullet+}$ – $Trp^{\bullet}$) difference spectrum calculated from the literature spectra in Fig. 2b and normalized to the spectrum of the 300-ns phase at ~580 nm. Inset, Deuterium isotope effect on the kinetics of the absorbance change at 580 nm. The H_2O sample contained 70 μM photolyase, 200 mM NaCl, 10% (w/w) glycerol and 20 mM Tris, pH 7.4. The D_2O sample was obtained by exchange of H_2O for D_2O (ref. 17) and addition of 10% (v/v) glycerol. Absorbance changes were recorded with a time resolution of 10 ns as described[16]. Excitation conditions and correction procedure were as in Fig. 2. **b**, Triangles, spectrum of the absorbance changes preceding the 300-ns phase (amplitude A in the inset of **a**). This spectrum was simulated (solid line) by addition of the $TrpH^{\bullet+}$ spectrum (Fig. 2b) and the ($FADH^{-}$ – $FADH^{\bullet}$) difference spectrum (dash-dotted line; for details, see Fig. 2a). Squares, spectrum of the absorbance changes after completion of the 300-ns phase, simulated (dashed line) by addition of the $Trp^{\bullet}$ spectrum (Fig. 2b) and the ($FADH^{-}$ – $FADH^{\bullet}$) difference spectrum. For the best simulations shown, the ($FADH^{-}$ – $FADH^{\bullet}$) differential molar absorption coefficient at 580 nm was assumed to be -2.4 times the molar absorption coefficient of $TrpH^{\bullet+}$ at 560 nm and –3.1 times that of $Trp^{\bullet}$ at 510 nm. **c**–**e**, Characterization of the deprotonation rate constant k_d of $TrpH^{\bullet+}$, obtained by least squares fits to flash-induced absorbance changes at 580 nm. Sample conditions: 30–70 μM photolyase and 200 mM NaCl; and 20 mM Tris pH 7.4 and glycerol at the concentrations indicated (**c**); Tris pH 7.4 or pH 8.4 at the concentrations indicated (**d**); or 20 mM buffer (pH 5.4, 6 and 6.5, MES; pH 7, 7.5, 8 and 8.5, Tris) (**e**).

with the difference between the solution spectra of $TrpH^{\bullet+}$ and $Trp^{\bullet}$, clearly indicating that the 300-ns phase reflects the deprotonation of $TrpH^{\bullet+}$. This conclusion is also supported by the kinetic isotope effect[18] observed upon exchange of H_2O for D_2O: $\tau(D_2O)/\tau(H_2O) = 2.2$ (see Fig. 3a, inset). As a consequence, the 300-ns phase should be preceded by electron transfer from TrpH to excited $FADH^{\bullet}$, forming $TrpH^{\bullet+}$ and $FADH^{-}$. Consistent with this prediction, the spectrum of the absorbance changes preceding the 300-ns phase (Fig. 3b, triangles) can be well simulated (solid line) by the addition of the $TrpH^{\bullet+}$ spectrum and the ($FADH^{-}$–$FADH^{\bullet}$) difference spectrum.

We conclude that the radical transfer from excited $FADH^{\bullet}$ to the tryptophan residue W306 occurs by fast (< 10 ns) electron transfer ($FADH^{\bullet}$*..TrpH $FADH^{-}$..$TrpH^{\bullet+}$), followed by deprotonation of $TrpH^{\bullet+}$ in about 300 ns. The nature of each of these two reactions will now be examined in more detail.

With respect to the deprotonation of the tryptophanyl radical, it is particularly important to identify the proton acceptor. Increasing glycerol concentration in the solvent causes a pronounced decrease in the rate of $TrpH^{\bullet+}$ deprotonation (Fig. 3c), suggesting that the proton from $TrpH^{\bullet+}$ is released to the solvent rather than being transferred to a proton accepting residue in the protein. The solvent contained two potential proton acceptors in sufficient concentration to account for a sub-microsecond reaction: unprotonated buffer molecules and H_2O itself. Increasing concentrations of Tris buffer accelerate the deprotonation of $TrpH^{\bullet+}$, and this acceleration is much more pronounced at pH 8.4 than at pH 7.4 (Fig. 3d), showing that the unprotonated Tris is the dominating proton acceptor at high concentrations of Tris. Extrapolation to zero Tris concentration yields a deprotonation rate constant, k_d, of about $5.3 \times 10^6\ s^{-1}$ which we attribute to proton transfer from $TrpH^{\bullet+}$ to H_2O in the solvent. Assuming $pK \approx 4$ for the deprotonating $TrpH^{\bullet+}$ in photolyase, this rate constant is consistent with the relationship $k_d = k_r \times 10^{-pK}\ s^{-1}$ for the deprotonation of weak acids in water, where k_r is the (diffusion controlled) reprotonation rate constant of typically 10^{10}–$10^{11}\ M^{-1}\ s^{-1}$ (see ref. 19 for a treatment of proton transfer processes in aqueous media). At the buffer concentration of 20 mM used in all our other experiments, H_2O should still be the dominating proton acceptor (see Fig. 3d). Varying the pH between 5.4 and 8.5 at 20 mM buffer, the kinetics of deprotonation (Fig. 3e) and its amplitude (data not shown) were essentially constant, as expected for H_2O ($pK = -1.7$) as proton acceptor.

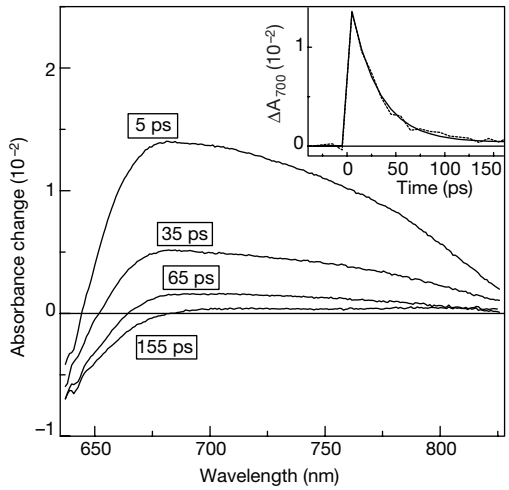

Figure 4 Study of the reaction $FADH^{\bullet}$*..TrpH $FADH^{-}$..$TrpH^{\bullet+}$ by ultrafast spectroscopy. Measurements were performed as described[26] with 620-nm pump pulses (70 fs full width at half maximum) and white-light continuum probe pulses, using a continuously moving thermostatted cell with an optical pathlength of 1 mm. Shown are transient spectra at selected delay times. Inset, kinetic data (dashed line) and exponential fit (solid line, τ = 29 ps) at 700 nm. The sample contained 260 μM photolyase, 200 mM NaCl, 15% (w/w) glycerol and 20 mM Tris, pH 7.4.

The kinetics of the electron transfer reaction starting from the excited state $FADH^{\bullet}$* were resolved by ultrafast pump-probe spectroscopy in the near-infrared spectral region where an induced absorption has been assigned to $FADH^{\bullet}$* (refs. 11, 20). Figure 4 shows typical difference spectra recorded at given delay times, and the kinetic trace at 700 nm. The broad absorbance increase between 650 nm and 800 nm observed immediately after excitation (5-ps spectrum), attributed to $FADH^{\bullet}$*, decays nearly completely with $\tau \approx 30$ ps (see 700-nm trace). The difference spectrum observed after completion of the 30-ps phase (see 155-ps spectrum) consists of a bleaching below 680 nm (the ground state absorption of $FADH^{\bullet}$) and is consistent with the presence of the state ($FADH^{-}$..$TrpH^{\bullet+}$) (see Fig. 3b). These results show that the excited state $FADH^{\bullet}$* decays in about 30 ps, presumably by abstracting an electron from a nearby tryptophan residue (see below).

Figure 5 depicts a reaction scheme for the radical transfer from excited $FADH^{\bullet}$ to W306 that is based on our results and takes into account essential elements of the X-ray structure of *E. coli* photolyase[21]. The solvent accessible tryptophan residue W306 is as far as 13.4 Å (shortest edge-to-edge distance) from the flavin, excluding a direct or superexchange-mediated electron transfer to $FADH^{\bullet}$* in 30 ps (refs. 7, 22). However, two other tryptophan residues, W382 and W359, are located in between (Fig. 5, inset), suggesting an electron transfer in three steps. The first step, downhill electron transfer from W382 to $FADH^{\bullet}$* takes 30 ps, the observed lifetime of $FADH^{\bullet}$* (Fig. 4). The next two steps, the presumably nearly isoenergetic electron transfers from W359 to the cation radical of W382 and from W306 to the cation radical of W359, should be faster than 10 ns because otherwise the deprotonation of the cation radical of W306, measured with a time resolution of 10 ns (Fig. 3a), should have shown a lag phase. Given the short distances between the partners (Fig. 5, inset), these three electron transfer rates are consistent with established rates of other intraprotein electron transfer reactions[7]. The proton release from the cation radical of W306 to the aqueous medium in about 300 ns is driven by a substantial decrease in free energy (about 0.2 eV at pH 7.4, assuming a pK of 4 for $TrpH^{\bullet+}$). This energetic stabilization is essential to trap the oxidizing radical on W306, which is accessible to exogenous reductants and sufficiently far apart from $FADH^{-}$ to prevent a fast direct recombination; moreover, the deprotonation creates a free energy barrier in a potential recombination pathway through repopulation of the cation radical of W306 and reverse electron transfer in the chain FAD–W382–W359–W306 (Fig. 5, broken arrows). The acceleration of the recombination with decreasing pH (Fig. 2a, inset) indicates that this is the actual recombination pathway.

Examination of the X-ray structure of *E. coli* photolyase[21] reveals important differences between the environments of the three tryptophans. The indole ring of W306 is partially surrounded by mainly polar amino acids. Its ring nitrogen is directly exposed to a shallow pocket that is open to the solvent and that can accommodate

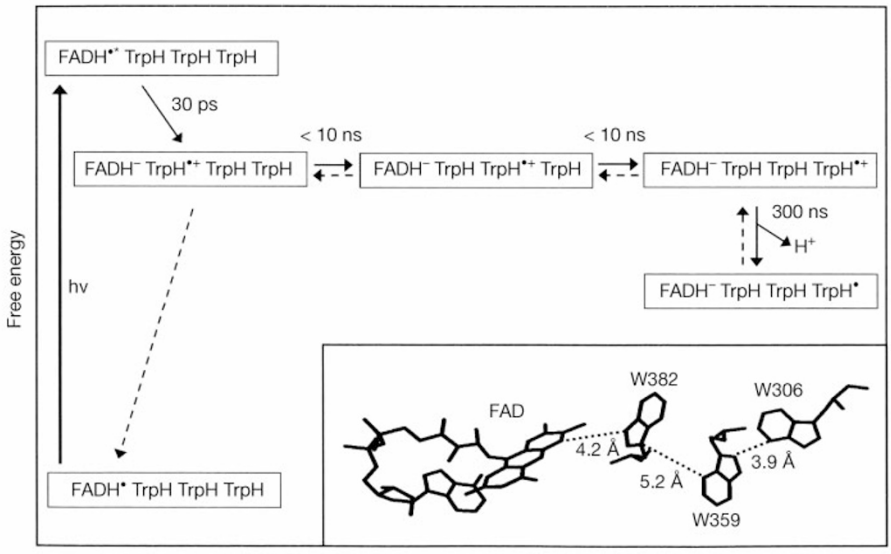

Figure 5 Reaction scheme for the radical transfer during photoactivation of *E. coli* photolyase. TrpH TrpH TrpH refers (from left to right) to W382, W359 and W306. Productive (forward) reactions are indicated as solid arrows, and back reactions as broken arrows. The free energy levels are not drawn to scale. We estimate the excited state of $FADH^{\bullet}$ to be ~2.0 eV above the ground state (corresponding to the energy of a 630-nm photon), and the ($FADH^{-}$ $TrpH^{\bullet+}$) states to be ~1.5 eV (assuming midpoint potentials of about –0.4 V for $FADH^{\bullet}$/$FADH^{-}$ in photolyase[27] and 1.1 V for $TrpH^{\bullet+}$/TrpH buried in a protein[14]). Inset, arrangement and shortest edge-to-edge distances between FAD, W382, W359 and W306 obtained from the X-ray structure of photolyase from *E. coli*[21]. Swiss-PdbViewer[28] was used to prepare the inset.

a water molecule, a situation that should favour proton transfer from the W306 cation radical to the solvent. In contrast, W382 is buried in the hydrophobic interior of the protein. There is no potential proton acceptor within 5 Å of the ring nitrogen of W382, excluding the possibility of deprotonation of the cation radical. The indole ring of W359 is surrounded by both hydrophobic and polar amino acids. The ring nitrogen appears to be hydrogen bonded to a more buried water molecule that might assist deprotonation of the W359 cation radical; however, our experimental data with a time resolution of 10 ns, together with previous data on the W306F mutant[12], do not give any indication for a deprotonation of the W359 cation radical.

The different polarities of the tryptophan environments should be relevant for the energetics of the electron transfer, as the reduction potential of the $TrpH^{\bullet+}$/TrpH couple is higher in a hydrophobic protein environment than in water[14]. For this reason, there is likely to be some decrease of the free energy of the $TrpH^{\bullet+}$ states in the order W382, W359, W306, favouring radical localization on W306 already, before its deprotonation.

A reaction scheme quite different from Fig. 5 was proposed previously[9]. It assumed that a long-lived quartet state of $FADH^{\bullet}$ (formed by intersystem crossing from the initial excited doublet state) abstracts an electron from W306 in about 500 ns, and that the resulting cation radical $TrpH^{\bullet+}$ remains protonated. This mechanism is incompatible with our results which establish unambiguously that $TrpH^{\bullet+}$ is formed in less than 10 ns and deprotonates in about 300 ns. The origin of the disagreement is most probably that the previous scheme was based on studies[11,20,23] using 355-nm laser flashes or Xe flashes that could excite species other than $FADH^{\bullet}$ (for example, fully oxidized FAD; see ref. 24). Under our excitation conditions, $FADH^{\bullet}$ is the only species being excited.

In summary, we have reached a consistent mechanism for the radical transfer during photoactivation of photolyase in which sequential electron transfer among amino-acid residues generates transient cation radicals before charge neutralization by proton release to the solvent. Thus, we conclude that charge compensating simultaneous proton transfer is not a prerequisite for intraprotein radical transfer. A definitive answer to the question of whether long-range radical transfer in other enzymes proceeds through a similar mechanism may require time-resolved methods to selectively monitor electron transfer, H-atom transfer and protonation/deprotonation events.

Our results on the activation of DNA photolyase from *E. coli* may be relevant for the other photolyases (class I and class II)[10] and also for the cryptochrome blue-light receptors in plants and animals, which are flavoproteins similar in sequence to photolyases[25]. Indeed, inspecting the aligned amino-acid sequences[10] of known photolyases and cryptochromes, we noticed that the tryptophan residues W382, W359 and W306 are uniformly conserved. This observation suggests that the electron transfer chain described here is involved in the function of all photolyases, and of blue light receptors as well. □

Received 30 December 1999; accepted 10 January 2000.

1. Stubbe, J. & van der Donk, W. A. Protein radicals in enzyme catalysis. *Chem. Rev.* **98,** 705–762 (1998).
2. Uhlin, U. & Eklund, H. Structure of ribonucleotide reductase protein R1. *Nature* **370,** 533–539 (1994).
3. Sjöberg, B.-M. The ribonucleotide reductase jigsaw puzzle: a large piece falls into place. *Structure* **2,** 793–796 (1994).
4. Siegbahn, P. E. M., Blomberg, M. R. A. & Crabtree, R. H. Hydrogen transfer in the presence of amino acid radicals. *Theor. Chem. Acc.* **97,** 289–300 (1997).
5. Siegbahn, P. E. M., Eriksson, L., Himo, F. & Pavlov, M. Hydrogen atom transfer in ribonucleotide reductase (RNR). *J. Phys. Chem.* **102,** 10622–10629 (1998).
6. Cukier, R. I. & Nocera, D. G. Proton coupled electron transfer. *Annu. Rev. Phys. Chem.* **49,** 337–369 (1998).
7. Page, C. C., Moser, C. C., Chen, X. & Dutton, P. L. Natural engineering principles of electron tunnelling in biological oxidation-reduction. *Nature* **402,** 47–52 (1999).
8. Sancar, A. No "end of history" for photolyases. *Science* **272,** 48–49 (1996).
9. Kim, S. -T., Heelis, P. F. & Sancar, A. Role of tryptophans in substrate binding and catalysis by DNA photolyase. *Methods Enzymol.* **258,** 319–343 (1995).
10. Yasui, A. & Eker, A. P. M. in *DNA Damage and Repair, Vol. 2: DNA Repair in Higher Eukaryotes* (eds Nickoloff, J. A. & Hoekstra, M. F.) 9–32 (Humana, Totowa, 1998).
11. Heelis, P. F., Okamura, T. & Sancar, A. Excited-state properties of *Escherichia coli* DNA photolyase in the picosecond to millisecond time scale. *Biochemistry* **29,** 5694–5698 (1990).
12. Li, Y. F., Heelis, P. F. & Sancar, A. Active site of DNA photolyase: tryptophan-306 is the intrinsic hydrogen atom donor essential for flavin radical photoreduction and DNA repair *in vitro*. *Biochemistry* **30,** 6322–6329 (1991).
13. Eker, A. P. M., Yajima, H. & Yasui, A. DNA photolyase from the fungus *Neurospora crassa*. Purification, characterization and comparison with other photolyases. *Photochem. Photobiol.* **60,** 125–133 (1994).
14. Tommos, C., Skalicky, J. J., Pilloud, D. L., Wand, A. J. & Dutton, P. L. *De novo* proteins as models of radical enzymes. *Biochemistry* **38,** 9495–9507 (1999).
15. Solar, S., Getoff, G., Surdhar, P. S., Armstrong, D. A. & Singh, A. Oxidation of tryptophan and N-methylindole by $N_3^{\bullet}$, $Br_2^{\bullet-}$, and $(SCN)_2^{\bullet-}$ radicals in light- and heavy-water solutions: A pulse radiolysis study. *J. Phys. Chem.* **95,** 3636–3643 (1991).
16. Aubert, C., Mathis, P., Eker, A. P. M. & Brettel, K. Intraprotein electron transfer between tyrosine and tryptophan in DNA photolyase from *Anacystis nidulans*. *Proc. Natl Acad. Sci. USA* **96,** 5423–5427 (1999).
17. Aubert, C., Brettel, K., Mathis, P., Eker, A. P. M. & Boussac, A. EPR detection of the transient tyrosyl radical in DNA photolyase from *Anacystis nidulans*. *J. Am. Chem. Soc.* **121,** 8659–8660 (1999).
18. Cleland, W. W., O'Leary, M. H. & Northrop, D. B. *Isotope Effects on Enzyme-Catalyzed Reactions* (Univ. Park Press, Baltimore, London, Tokyo, 1977).
19. Eigen, M. Proton transfer, acid-base catalysis, and enzymatic hydrolysis Part I: elementary processes. *Angew. Chem. Internat. Edn.* **3,** 1–19 (1964).
20. Okamura, T., Sancar, A., Heelis, P. F., Hirata, Y. & Mataga, N. Doublet-quartet intersystem crossing of flavin radical in DNA photolyase. *J. Am. Chem. Soc.* **111,** 5967–5969 (1989).
21. Park, H. W., Kim, S. T., Sancar, A. & Deisenhofer, J. Crystal structure of DNA photolyase from *Escherichia coli*. *Science* **268,** 1866–1872 (1995).
22. Cheung, M. S., Daizadeh, I., Stuchebrukhov, A. A. & Heelis, P. F. Pathways of electron transfer in *Escherichia coli* DNA photolyase: Trp^{306} to FADH. *Biophys J.* **76,** 1241–1249 (1999).
23. Kim, S. T., Sancar, A., Essenmacher, C. & Babcock, G. T. Time-resolved EPR studies with DNA photolyase: excited-state $FADH^0$ abstracts an electron from Trp-306 to generate $FADH^-$, the catalytically active form of the cofactor. *Proc. Natl Acad. Sci. USA* **90,** 8023–8027 (1993).
24. Gindt, Y. M. *et al.* Origin of the transient electron paramagnetic resonance signals in DNA photolyase. *Biochemistry* **38,** 3857–3866 (1999).
25. Cashmore, A. R., Jarillo, J. A., Xu, Y. -J. & Liu, D. Cryptochromes: blue light receptors for plants and animals. *Science* **284,** 760–765 (1999).
26. Martin, J.-L. & Vos, M. H. Femtosecond measurements of geminate recombination in heme proteins. *Methods Enzymol* **232,** 416–430 (1994).
27. Heelis, P. F., Deeble, D. J., Kim, S. T. & Sancar, A. Splitting of cys-syn cyclobutane thymine–thymine dimers by radiolysis and its relevance to enzymatic photoreactivation. *Int. J. Radiat. Biol.* **62,** 137–143 (1992).
28. Guex, N. & Peitsch, M. N. SWISS-MODEL and the Swiss-PdbViewer: An environment for comparative protein modeling. *Electrophoresis* **18,** 2714–2723 (1997).

Acknowledgements

We thank A. Yasui for providing us with the *E. coli* photolyase expression construct; P. Barth and P. L. Dutton for helpful discussions; and T. A. Mattioli for critical reading of the manuscript. M.H.V. is supported by CNRS.

Correspondence and requests for materials should be addressed to K.B. (e-mail: brettel@dsvidf.cea.fr).

Engineering stability in gene networks by autoregulation

Attila Becskei & Luis Serrano

EMBL, Structures & Biocomputing, Meyerhofstrasse 1, Heidelberg D-69012, Germany

The genetic and biochemical networks which underlie such things as homeostasis in metabolism and the developmental programs of living cells, must withstand considerable variations and random perturbations of biochemical parameters[1–3]. These occur as transient changes in, for example, transcription, translation, and RNA and protein degradation. The intensity and duration of these perturbations differ between cells in a population[4]. The unique state of cells, and thus the diversity in a population, is owing to the different environmental stimuli the individual cells experience and the inherent stochastic nature of biochemical processes (for example, refs 5 and 6). It has been proposed, but not

K. Meijer, D. Dudek, A. Ahn, T. Kubow and J. Hearst for comments on earlier drafts, E. Florance for electron microscopy, the University of California Museum of Paleontology electron microscope laboratory and the Scientific Visualization Center at Berkeley.

Correspondence and requests for materials should be addressed to R.J.F. (e-mail: rjfull@socrates.berkeley.edu).

Neural synchrony correlates with surface segregation rules

Miguel Castelo-Branco, Rainer Goebel, Sergio Neuenschwander & Wolf Singer

Max-Planck-Institut für Hirnforschung, Deutschordenstraße 46, 60528 - Frankfurt am Main, Germany

To analyse an image, the visual system must decompose the scene into its relevant parts. Identifying distinct surfaces is a basic operation in such analysis, and is believed to precede object recognition[1,2]. Two superimposed gratings moving in different directions (plaid stimuli) may be perceived either as two surfaces, one being transparent and sliding on top of the other (component motion) or as a single pattern whose direction of motion is intermediate to the component vectors (pattern motion)[3–6]. The degree of transparency, and hence the perception, can be manipulated by changing only the luminance of the grating intersections[7–12]. Here we show that neurons in two visual cortical areas—A18 and PMLS—synchronize their discharges when responding to contours of the same surface but not when responding to contours belonging to different surfaces. The amplitudes of responses correspond to previously described rate predictions[3,13–16] for component and pattern motion, but, in contrast to synchrony, failed to reflect the transition from component to pattern motion induced by manipulating the degree of transparency. Thus, dynamic changes in synchronization could encode, in a context-dependent way, relations among simultaneous responses to spatially superimposed contours and thereby bias their association with distinct surfaces.

Specialized visual neurons may signal the motion of either the individual gratings of a plaid (component-selective cells) or of the global pattern (pattern-selective cells). For the identification of these cells, responses evoked by single gratings were compared to those evoked by unambiguous plaid patterns moving in an intermediate direction, and the results indicate that both cell types exist[3,13–16]. However, except for a single study in the motion sensitive area (MT)of monkey visual cortex[11], no attempt has been made to investigate changes in response amplitudes associated with gradual modifications of transparency conditions. Therefore, little is known about how well individual cells differentiate between component and pattern motion.

Here, we investigate this question with multi-electrode recordings from neurons located in areas A18 and PMLS (postero-medial bank of the lateral suprasylvian sulcus) of the cat visual cortex. In addition, we use cross-correlation analysis to examine the hypothesis that binding of the moving contours into one coherent pattern or two independently moving gratings is associated with changes in the synchronization of responses.

Neurons synchronize their discharges with a precision in the millisecond range if they are activated by single contours, but they do not synchronize when activated by contours of different objects[17–20]. It has been proposed, therefore, that synchronization serves as a binding mechanism by virtue of selectively raising the saliency of the synchronized discharges and thereby favouring their joint processing at subsequent levels. Accordingly, when exposed to plaid stimuli, cells responding to contours of the same surface should synchronize their responses, and cells activated by contours belonging to different surfaces should not synchronize. Which cells are associated with a particular surface depends on transparency conditions, on the match of the cells' preferred direction of motion with the direction of motion of the plaid components and on the spatial relation (overlap, colinearity) of the receptive fields (RFs). In pattern motion, all cells capable of responding to the respective component motions should synchronize their responses because they are excited by contours of the same surface. In component motion, only those cells that respond to the contours of the same component grating should synchronize. This synchronization

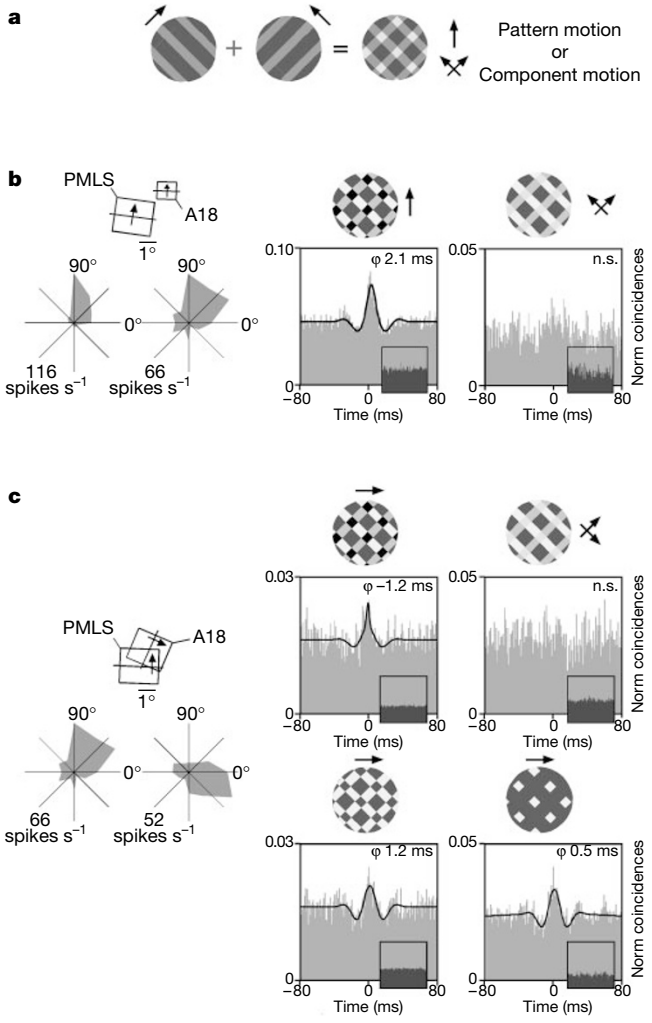

Figure 1 Dependence of synchrony on transparency conditions and receptive field (RF) configuration. **a**, Stimulus configuration. **b**, Synchronization between neurons with non-overlapping RFs and similar directional preferences recorded from A18 and PMLS. Left, RF constellation and tuning curves; right, cross-correlograms for responses to a non-transparent (left) and transparent plaid (right) moving in the cells' preferred direction. Grating luminance was asymmetric to enhance perceptual transparency[3]. Small dark correlograms are shift predictors. **c**, Synchronization between neurons with different direction preferences recorded from A18 (polar and RF plots, left). Top, correlograms of responses evoked by a non-transparent (left) and a transparent (right) plaid moving in a direction intermediate to the cells' preferences. Bottom, correlograms of responses evoked by a non-transparent plaid with reversed contrast conditions (left), and by a surface defined by coherent motion of intersections (right). Scale on polar plots: discharge rate in spikes per second. Scale on correlograms: abscissa, shift interval in ms, bin width 1 ms; ordinate, number of coincidences per trial, normalized. Thick line, fitted gabor function; φ, phase shift. n.s., not significant.

should be particularly robust for cells with colinearly aligned, overlapping RFs as these respond to the same bar of a component grating.

Results of experiments addressing these predictions for cell pairs with different RF configurations are shown in Figs 1–3. Population data are presented in Fig. 4. Figure 1b shows neurons with non-overlapping and non-colinear RFs that have similar direction preference and were recorded simultaneously from areas A18 and PMLS. These cells synchronized in response to non-transparent patterns moving in the neurons' preferred direction but not when activated by a transparent plaid. Figure 1c (top) shows A18 neurons with non-overlapping RFs and different direction preferences. These cells too synchronized in the non-transparent condition when the direction of pattern motion was intermediate between the cells' preferred directions but not in the transparent condition. The synchronization in the non-transparent condition was of similar magnitude for all contrast conditions that bias perception towards pattern motion (Fig. 1c, compare top and bottom).

Figure 2 shows cells recorded from PMLS that had similar direction preferences and colinearly aligned overlapping RFs. These cells synchronized when activated with a single grating moving in their preferred direction and they continued to discharge in synchrony when another grating of different orientation and direction of motion was superimposed, even when transparency conditions were optimal for component motion. This indicates, as predicted, that the responses at both sites had remained associated with contours of the same surface.

To determine whether the degree of synchrony observed with plaids can be accounted for by linear summation of the synchrony induced by each grating alone, we calculated a linear predictor from the sum of coincidences evoked by each grating alone. For neuron pairs with colinear, overlapping RFs (Fig. 2a), synchrony to plaids did indeed correspond to the linear predictor. This was not so for cells with more discordant RFs and differing direction preferences (Fig. 2b). Their responses exhibited strong synchrony when evoked with one of the two gratings but this synchrony broke down when a second transparent grating was superimposed, indicating that addition of the second grating caused active desynchronization. As predicted, cells at the two sites now respond independently to contours of different surfaces.

To exclude the possibility that the changes in synchronization induced by modifications of transparency were due to local contrast changes at the grating intersections rather than to global segmentation processes, we induced the transition from pattern to component motion by changing the ratio (duty cycle) between the width of white and dark bars of the gratings[1,9] (Fig. 3, top). In this case, a gradual change in stimulus parameters leads to an abrupt change in figure–ground assignment. Non-transparent grating intersections suddenly change to background (figure–ground reversal) and this is associated with a sudden switch in perception from pattern to component motion[1,9]. These modifications in duty cycle induce exactly the same changes in synchrony as modifications of transparency conditions by contrast manipulation of intersections (Fig. 3). The relations between synchronization strength, the transparency condition, the direction of plaid motion and the direction preferences of the neuron pairs conform to the predictions (Fig. 3b and c). Cells with differing direction preferences synchronize maximally with non-transparent patterns moving in directions intermediate to the respective preferred directions, but synchrony breaks down when the plaid becomes transparent (Fig. 3b). Some residual synchrony remains when the plaid moves in the opposite direction. In this case synchrony changes only little with transparency, indicating that now both sites respond mainly to contours of one grating. By contrast, synchrony among cells with overlapping, colinearly aligned RFs remains unaffected by changes in transparency. Synchrony varies with the direction of plaid movement but similarly for transparent and non-transparent plaids (Fig. 3c). This agrees with prediction as responses of cells with colinear RFs always remain associated with a single contour that may be either part of a pattern, or one of the two component gratings.

The perceptual switch between component and pattern motion is abrupt. To determine whether this is also the case for synchronization we measured correlation strength with a sliding window analysis while introducing gradual changes of duty cycle. For cells with different direction preference, synchronization broke down abruptly when the pattern became transparent. Correlation peaks

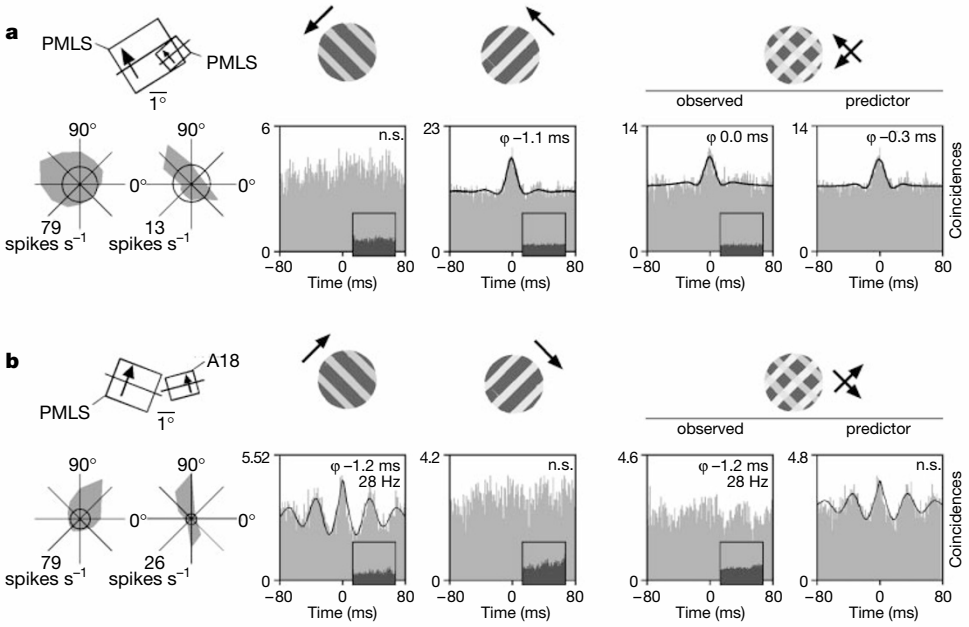

Figure 2 Comparison between single gratings and plaids. **a**, Synchronization between neurons with similar direction preferences and colinearly arranged, spatially contiguous RFs recorded from area PMLS. Correlograms are from responses to single gratings moving in the cells' non-preferred (first) and preferred direction (second) and from responses to a transparent plaid resulting from a superposition of the two gratings (third correlogram). The fourth correlogram corresponds to the linear predictor. **b**, Same analysis as in **a** for neurons with spatially segregated RFs and differing direction preferences recorded from areas A18 and PMLS. Conventions as in Fig. 1.

remained high and unchanged during the first half of the duty cycle change and then dropped abruptly below the level of significance. By contrast, responses of cells with colinearly aligned, overlapping RFs remained synchronized throughout the change in duty cycle (Fig. 3d).

Classifying cells as component or pattern selective (see Methods and refs 13–16) confirmed that most cells in areas A18 and PMLS of cat visual cortex are best described as component selective (Fig. 4 top and refs 14–16). Furthermore, classification of cells into component- and pattern-selective subsets changed only little when response profiles were obtained with transparent and non-transparent plaids, respectively, indicating that individual cells do not differentiate between transparent and non-transparent conditions (Fig. 4a). To quantify this result, we subtracted the responses obtained with the two different plaid constellations from each other (component minus pattern condition) and reclassified the cells (Fig. 4, top right). Almost none of the resulting data points had any significant correlation with either of the two predictors. This proves that there is no systematic relation between rate changes of neurons in A18 and PMLS and transparency modifications.

Thus, differential synchronization might be the signal that biases perception towards component or pattern motion. To quantify stimulus-dependent changes in synchrony, we performed a split-plot analysis of variance (ANOVA). Synchronization strength was evaluated for each cell pair for responses evoked with single gratings and for responses evoked with both transparent and non-transparent plaids moving in the direction intermediate to those preferred by the respective cells. In the analysis, we also included a linear predictor of synchrony that corresponds to the correlation strength that one expects for plaids if correlations result simply from the sum of the coincidences in the responses to the respective single gratings. Correlation strength determined for the various conditions (pattern, component, single grating and linear predictor) was then related in a multifactorial analysis to the RF configuration of the analysed cell pairs. The following parameters were considered: RF overlap, colinearity of fields with similar direction preferences and difference between direction preferences. This analysis showed no detectable difference between cell pairs distributed within or across areas A18 and PMLS, so we pooled the data from all cell pairs. As predicted, responses of neuron pairs whose RFs differed in all the chosen categories (position, colinearity and direction preference) exhibit a highly significant reduction in synchrony when plaids undergo modifications that bias perception from pattern to component motion ($P \ll 0.01$, split-plot ANOVA, Fig. 4b). Conversely, no significant changes in synchrony ($P > 0.3$) occurred for cell pairs whose RFs had the same direction preference and were in addition either overlapping or colinear, conditions in which responses are likely to result from the same contour.

To illustrate the dependence of synchrony on both the transparency condition and the direction of plaid motion, we plotted synchronization strength against direction of plaid motion for transparent and non-transparent plaids as well as for a single grating (Fig. 4c). In this analysis we included only cells with strong direction preferences ($n = 25$) but pooled all pairs with similar and differing direction preferences. Differences in synchronization were maximal when plaid motion was in the direction intermediate to those preferred by the respective cells, the 'zero' direction. In this case non-transparent plaids induced strong synchronization whereas transparent plaids caused a complete break down of synchrony. When the direction of movement was offset from 'zero' by more than 30°, when one of the component gratings moved in a direction close to 'zero', differences between transparent and non-transparent conditions were less pronounced, because cells whose direction preference differed by less than 20° synchronized in both conditions. Single gratings induced synchrony at all directions of motion that evoked strong responses at both sites. This indicates that transparent plaids moving in 'zero' direction induce active desynchronization of

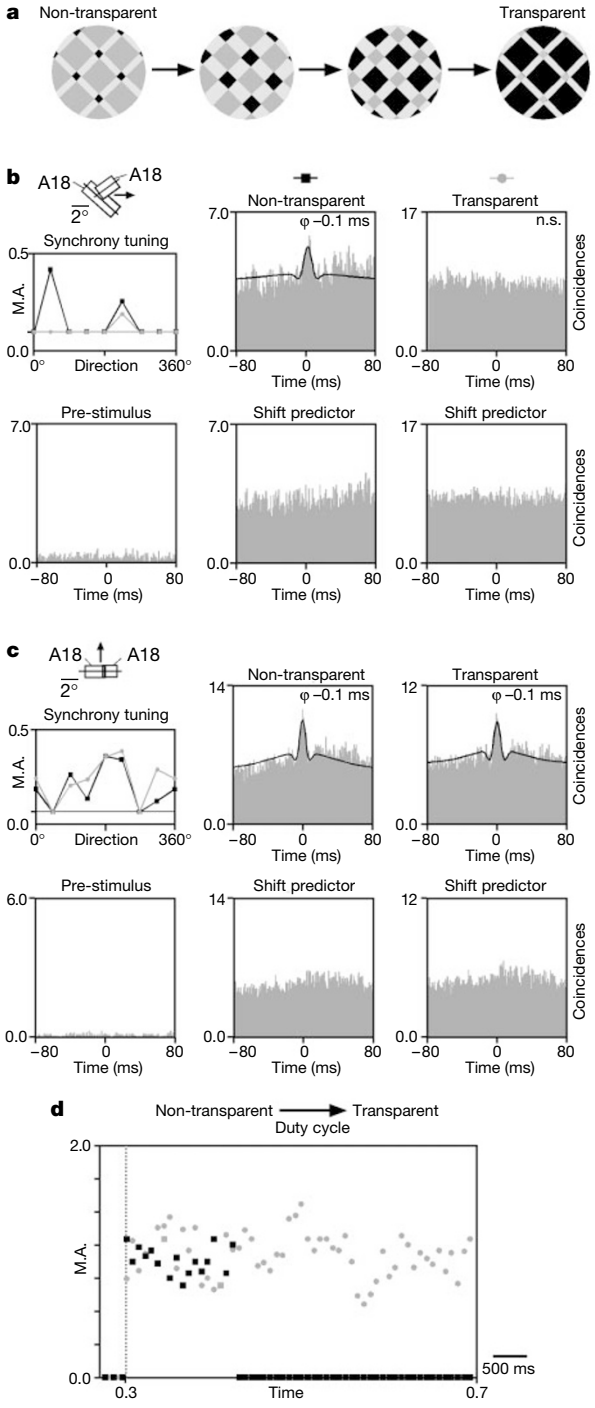

Figure 3 Changes in synchrony induced by manipulating the duty cycle of plaid components. **a**, A progressive change in duty cycle induces a change from non-transparent to transparent motion because of a flip in foreground–background assignment[1,9]. **b**, **c**, Dependence of synchrony on the direction of plaid motion and transparency conditions for two cell pairs in A18 with discordant (**b**) and concordant (**c**) RFs. Left (synchrony tuning), relative modulation amplitude (MA) of correlation peaks for different directions of plaid motion (abscissa: 0°, horizontal right; 90°, vertical up) for non-transparent (dark squares) and transparent (grey circles) plaids. Middle and right, cross-correlograms for responses to non-transparent and transparent plaids moving in a direction intermediate between the cells' preferences (**b**) and in the cells' preferred direction (**c**). Bottom, pre-stimulus correlograms and shift predictors. **d**, Sliding window analysis (step 100 ms, window 400 ms) of changes of correlation strength (ordinate) resulting from duty cycle modifications (between 0.7 and 0.3, abscissa) for the cell pairs shown in **b** (black squares) and **c** (grey circles).

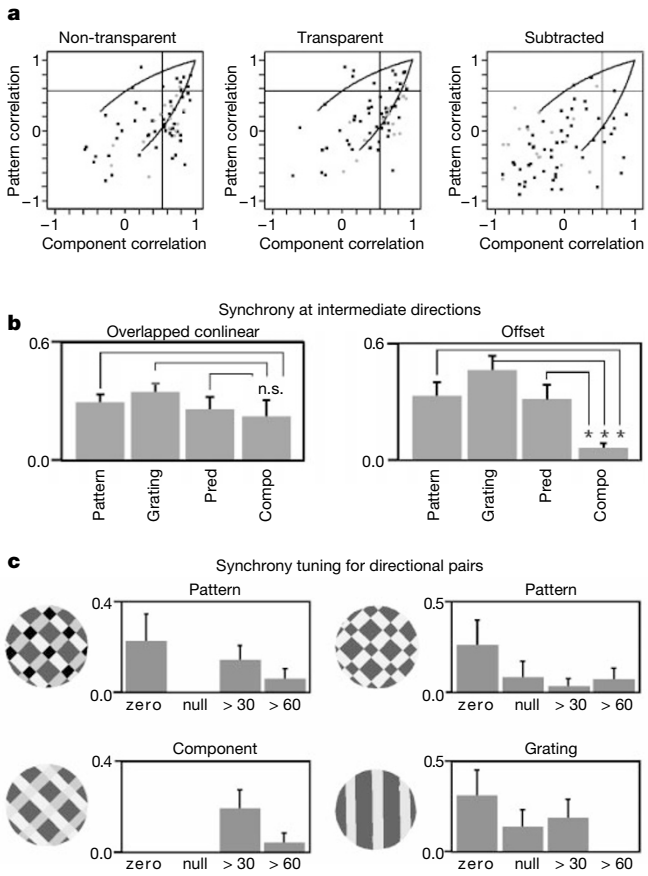

Figure 4 Effect of transparency manipulation on response amplitudes and synchrony. **a**, Scatter plots identifying cells as component (abscissa) or pattern selective (ordinate) obtained from responses to non-transparent (left) and transparent plaids (middle). Continuous lines indicate significance of classification. Cells in upper left and lower right cases are classified as pattern and component selective, respectively. Cells outside these regions or inside the curved area are unclassified. Right, classification after subtraction of responses to non-transparent plaids from those to transparent plaids. Dark squares and grey circles, stimuli in which either the duty cycle (squares) or the luminance of intersections (circles) have been manipulated. **b**, Comparison of correlation strength (ordinate) for non-transparent (pattern) and transparent (component) plaids, single gratings (grating) and the linear predictor (pred) for cell pairs with overlapping, colinear (top) and non-overlapping, dissimilar RFs (bottom). Responses were evoked with plaids (gratings) moving in a direction intermediate to those preferred by the respective cells. **c**, Dependence of correlation strength (ordinate) on stimulus conditions (pattern, component, grating) and direction of stimulus motion (abscissa) for the subset of cells with strong directional preferences ($n = 25$). Zero, stimuli moving in a direction intermediate ($\pm$ 30°) to the cells' preferred directions; null, direction opposite to zero; $>$ 30 and $>$ 60, directions offset by at least 30° or 60° from zero.

cells responding to the respective components.

In early visual areas such as those investigated here, most cells are component specific and, as our data indicate, their rate-modulated responses do not distinguish between pattern and component motion conditions[13–16]. This calls for a transparency-sensitive, rate-independent grouping cue that permits subsequent processing stages to associate responses with either a single or two different surfaces. We propose that the differential synchronization of the responses of component-selective cells described here could serve as the required grouping signal, because synchrony occurred selectively among exactly those responses that need to be bound to account for the different perceptions induced by plaids of different transparency.

For the read-out of these differential synchronization patterns, two non-exclusive possibilities may be considered. Coincidence detectors in higher processing areas could transform the synchronized output of cells in A18 and PMLS in rate codes for the various surfaces in plaid stimuli. Alternatively, the synchronously active ensembles of neurons distributed across areas A18 and PMLS, and presumably also other cortical areas, could themselves serve as the distributed representations of the surfaces. Changes in cortical synchronization patterns are sensed by output structures such as the optic tectum[21] and can thus lead to modification of eye movements without requiring further decoding[22].

In conclusion, the present findings provide evidence that synchronization correlates well with the perceptual segmentation of a complex visual pattern into distinct, spatially overlapping surfaces. As no such correlation was found for the rate-modulated responses of neurons in the cortical areas analysed here, we propose that synchronization serves to group responses for further joint evaluation. □

Methods

Anaesthesia was induced with ketamine (Ketanest, Parke–Davis, 10 mg kg^{-1}, intramuscular) and xylazine (Rompun, Bayer, 2 mg kg^{-1}, intramuscular), and maintained with a mixture of 70% N_2O and 30% O_2 supplemented by 0.5–1.0% halothane. Paralysis was obtained with pancuronium bromide (Pancuronium, Organon, 0.15 mg kg^{-1} h^{-1}). Single- or multi-unit activity (306 recording pairs in six animals) was recorded with multiple (up to four) varnish-coated tungsten electrodes[23]. Cortical areas A18 and PMLS were identified on the basis of RF properties and histology[24]. Signals were band-pass filtered from 1 to 3 kHz and spikes were detected with an amplitude discriminator with the threshold set to twice the noise level.

Visual stimuli were generated on a computer screen (refresh rate of 100 Hz). Squarewave gratings were superimposed in a circular display subtending 12–18° of visual angle. Transparent and non-transparent plaids were interleaved with single gratings and moved in up to twelve different directions, movement direction changing from trial to trial in a pseudorandom sequence (20 trials per configuration).

Plaid velocities (pattern velocity, 8 and 16° s^{-1}), background, grating and intersection luminances (0.5–140 cd m^{-2}, mean stimulus luminance ~35 cd m^{-2}), duty cycle (around 0.3) and angle between gratings (preferably above 135°) were adjusted to induce strong perceptual biases. Stimulus conditions were validated by analysing eye movements from

electro-oculographic recordings in two awake cats and this indicated that the animals distinguished between component and pattern motion.

Auto- and cross-correlograms were calculated for responses from individual trials with a resolution of 1.0 ms and averaged over 20 stimulus presentations. Pre-stimulus correlograms controlled for stimulus independent correlations and shift predictors for synchronization induced by stimulus-locking[25]. A damped cosine function was fitted to the correlograms to quantify the strength and phase shift of correlations and the frequency and modulation depth of oscillatory patterning[23,26]. Correlation strength was assessed from the modulation amplitude (MA), the ratio between the amplitude of the central peak of both the fitted and the raw function (as a control) and the correlogram offset. MA values obtained with and without normalization to the geometric mean of firing rates (normalized coincidences) gave similar results.

A split-plot design[27] was applied (ANOVA for repeated measures) to evaluate correlation strength as a function of stimulus (pattern and component motion, single gratings, linear predictor derived from responses to single gratings) and RF configuration. Orientation and direction preferences, and tuning width were determined with vector averaging methods[28,29]. Recording sites were classified as having similar orientation preferences if these differed by less than 20°, as having colinear RFs if the offset of the axial alignment of the RFs was $<$ 20% of the size of the smaller RF, and as having overlapping RFs if discharge regions (mapped with small moving bars) overlapped. RFs were classified as directional if the ratio of responses to stimuli in preferred and non-preferred directions was $\geqslant 2$ (true for 106 pairs). 55 pairs differed and 16 pairs matched in all categories; 25 pairs exhibited strong directional tuning at both sites.

Based on firing rate, neurons were classified as component selective if the directional tuning curve obtained with plaids correlated with that resulting from linear summation of the responses to the respective component gratings. Conversely, cells were classified as pattern-selective if the tuning curve obtained with a plaid correlated better with that resulting from stimulation with a single grating. Computation of statistical boundaries took into account the number of stimulus directions and the number of stimulus trials. The partial correlations were computed with the following equation: $R_p = (r_p - r_c r_{pc})/[(1 - r_c^2)(1 - r_{pc}^2)]^{1/2}$. R_p, partial correlation coefficient for the pattern prediction; r_c, correlation coefficient between the plaid response and the component model; r_p, correlation coefficient between the plaid response and the pattern model; r_{pc}, correlation coefficient for the two models. Also R_c is the partial correlation coefficient for the component prediction, obtained by interchanging r_p and r_c[13].

Received 24 January; accepted 11 April 2000.

1. Stoner, G. R. & Albright, T. D. The interpretation of visual motion: evidence for surface segmentation mechanisms. *Vision Res.* **36,** 1291–1310 (1996).
2. Shimojo, S., Silverman, G. H. & Nakayama, K. An occlusion-related mechanism of depth perception based on motion and interocular sequence. *Nature* **333,** 265–268 (1988)
3. Movshon, J. A, Adelson, E. H., Gizzi, M. & Newsome, W. T. in *Study Group on Pattern Recognition Mechanisms* (eds Chagas, C. Gatass, R. & Gross, C. G.) (Pontifica Academia Scientiarum, Vatican City, 1985).
4. Adelson, E. H. & Movshon, J. A. Phenomenal coherence of moving visual patterns. *Nature* **300,** 523–525 (1982).
5. Stoner, G. R., Albright, T. D. & Ramachandran, V. S. Transparency and coherence in human motion perception. *Nature* **344,** 153–155 (1990)
6. Smith, A. T. & Harris, L. R. Use of plaid patterns to distinguish the corticofugal and direct retinal inputs to the brainstem optokinetic nystagmus generator. *Exp. Brain Res.* **86,** 324–332 (1991).
7. Metelli, F. The perception of transparency. *Sci. Am.* **230,** 90–98 (1974).
8. Beck, J. & Ivry, R. On the role of figural organization in perceptual transparency. *Percept. Psychophys.* **44,** 585–594 (1988).
9. Albright, T. D. & Stoner, G. R. Visual motion perception. *Proc. Natl Acad. Sci. USA* **92,** 2433–2440 (1995).
10. Stoner, G. R. & Albright T. D. Luminance contrast affects motion coherency in plaid patterns by acting as depth from occlusion cue. *Vision Res.* **38,** 387–401 (1998).
11. Stoner, G. R. & Albright, T. D. Neural correlates of perceptual motion coherence. *Nature* **358,** 412–414 (1992).
12. Castelo-Branco, M. *et al.* MT/MST activation depends on the interpretation of stimuli: a functional fMRI study of the perception of plaids. *Soc. Neurosci. Abstr.* **23,** 460 (1997).
13. Rodman, H. R. & Albright, T. D. Single-unit analysis of pattern-motion selective properties in the middle temporal visual area (MT). *Exp. Brain Res.* **75,** 53–64 (1989).
14. Gizzi, M. S., Katz, E., Schumer, R. A. & Movshon, J. A. Selectivity for orientation and direction of motion of single neurons in cat striate and extrastriate visual cortex. *J. Neurophysiol.* **63,** 1529–1543 (1990).
15. Scannell, J. W. *et al.* Visual motion processing in the anterior ectosylvian sulcus of the cat. *J. Neurophysiol.* **76,** 895–907 (1996).
16. Merabet, L., Desautels, A., Minville, K. & Casanova, C. Motion integration in a thalamic visual nucleus. *Nature* **396,** 265–268 (1998).
17. Gray, C. M., Konig, P., Engel, A. K. & Singer, W. Oscillatory responses in cat visual cortex exhibit inter-columnar synchronization which reflects global stimulus properties. *Nature* **338,** 334–337 (1989).
18. Engel, A. K., Konig, P., Kreiter, A. K. & Singer, W. Interhemispheric synchronization of oscillatory neuronal responses in cat visual cortex. *Science* **252,** 1177–1179 (1991).
19. Freiwald, W. A., Kreiter, A. K. & Singer, W. Stimulus dependent intercolumnar synchronization of single unit responses in cat area 17. *NeuroReport* **6,** 2348–2352 (1995).
20. Kreiter, A. K. & Singer, W. Stimulus-dependent synchronization of neuronal responses in the visual cortex of the awake macaque monkey. *J. Neurosci.* **16,** 2381–2396 (1996).
21. Brecht, M., Singer, W. & Engel, A. K. Correlation analysis of corticotectal interactions in the cat visual system. *J. Neurophysiol.* **79,** 2394–2407 (1998).
22. Brecht, M., Singer, W. & Engel, A. K. Collicular saccade vectors defined by synchronization. *Soc. Neurosci. Abstr.* **23,** 843 (1997).
23. Castelo-Branco, M., Neuenschwander, S. & Singer, W. Synchronization of visual responses between the cortex, lateral geniculate nucleus, and retina in the anesthetized cat. *J. Neurosci.* **18,** 6395–6410 (1998).
24. Palmer, L. A., Rosenquist, A. C. & Tusa, R. J. The retinotopic organization of lateral suprasylvian visual areas in the cat. *J. Comp. Neurol.* **177,** 237–256 (1978).
25. Perkel, D. H., Gerstein, G. L. & Moore, G. P. Neuronal spike trains and stochastic point processes. II. Simultaneous spike trains. *Biophys. J.* **7,** 419–440 (1967).
26. König, P. A method for the quantification of synchrony and oscillatory properties of neuronal activity. *J. Neurosci. Methods* **54,** 31–37 (1994).
27. Edwards, A. L. *Multiple Regression Analysis and the Analysis of Variance and Covariance* (W. H. Freeman, New York, 1985).
28. Batschelet, E. *Circular Statistics in Biology* (Academic, London, 1993).
29. Swindale, N. V. Orientation tuning curves: empirical description and estimation of parameters. *Biol. Cybern.* **78,** 45–56 (1998).

Acknowledgements

We thank H. Klon-Lipok, P. Janson and S. Grimm for their technical assistance in electrode manufacture and histology. This research was sponsored by the Max-Planck-Gesellschaft. M.C.-B. was partially supported by the Gulbenkian Foundation and Programa Praxis, Portugal.

Correspondence and requests for materials should be addressed to: W.S. (e-mail: singer@mpih-frankfurt.mpg.de).

Photoactivated γ-secretase inhibitors directed to the active site covalently label presenilin 1

Yue-Ming Li*, Min Xu*, Ming-Tain Lai*, Qian Huang*, José L. Castro†, Jillian DiMuzio-Mower*, Timothy Harrison†, Colin Lellis*, Alan Nadin†, Joseph G. Neduvelil†, R. Bruce Register*, Mohinder K. Sardana*, Mark S. Shearman†, Adrian L. Smith†, Xiao-Ping Shi*, Kuo-Chang Yin*, Jules A. Shafer* & Stephen J. Gardell*

** Department of Biological Chemistry, Merck Research Laboratories, West Point, Pennsylvania 19486, USA*
† Neuroscience Research Centre, Merck Sharp & Dohme Research Laboratories, Terlings Park, Harlow, Essex CM20 2QR, UK

Cleavage of amyloid precursor protein (APP) by the β- and γ-secretases generates the amino and carboxy termini, respectively, of the Aβ amyloidogenic peptides Aβ40 and Aβ42—the major constituents of the amyloid plaques in the brain parenchyma of Alzheimer's disease patients[1]. There is evidence that the polytopic membrane-spanning proteins, presenilin 1 and 2 (PS1 and PS2), are important determinants of γ-secretase activity: mutations in PS1 and PS2 that are associated with early-onset familial Alzheimer's disease[2,3] increase the production of Aβ42 (refs 4–6), the more amyloidogenic peptide; γ-secretase activity is reduced in neuronal cultures derived from PS1-deficient mouse embryos[7]; and directed mutagenesis of two conserved aspartates in transmembrane segments of PS1 inactivates the ability of γ-secretase to catalyse processing of APP within its transmembrane domain[8]. It is unknown, however, whether PS1 (which has little or no homology to any known aspartyl protease) is itself a transmembrane aspartyl protease or a γ-secretase cofactor, or helps to colocalize γ-secretase and APP. Here we report photoaffinity labelling of PS1 (and PS2) by potent γ-secretase inhibitors that were designed to function as transition state analogue inhibitors directed to the active site of an aspartyl protease. This observation indicates that PS1 (and PS2) may contain the active site of γ-secretase. Interestingly, the intact, single-chain form of wild-type PS1 is not labelled by an active-site-directed photoaffinity probe, suggesting that intact wild-type PS1 may be an aspartyl protease zymogen.

We used L-685,458 (Fig. 1), a potent γ-secretase inhibitor[9], to prepare photoaffinity probes that label the active site of γ-secretase.